

Production of Spin-Polarized Molecular Beams via Microwave or Infrared Rotational Excitation

Chrysovalantis S. Kannis^a, T. Peter Rakitzis^{b,c,*}

^a*Institut für Laser- und Plasmaphysik, Heinrich-Heine-Universität Düsseldorf, Universitätsstraße 1, Düsseldorf, 40225, NRW, Germany*

^b*Department of Physics, University of Crete, Heraklion-Crete, 70013, Greece*

^c*Institute of Electronic Structure and Lasers, Foundation for Research and Technology-Hellas, N. Plastira 100, Heraklion-Crete, 71110, Greece*

Abstract

We show how small molecules in an intense and cold molecular beam can be highly nuclear-spin polarized via microwave or infrared rotational excitation schemes, followed by hyperfine-induced quantum beats. Repumping schemes can be used to achieve polarization above 90% in cases where single-pumping schemes are insufficient. Projected production rates in excess of 10^{21} s^{-1} allow applications including nuclear-magnetic-resonance signal enhancement, and spin-polarized nuclear fusion, where polarized nuclei are known to enhance D-T and D- ^3He fusion cross sections by 50%.

Keywords: Hyperpolarization, Infrared excitation, Microwave excitation, NMR/ESR signal enhancement, Spin-polarized fusion

1. Introduction

The production of spin-polarized molecules is important in several fields, including the study of spin-dependent effects in particle and nuclear physics [1], and in applications of nuclear magnetic resonance in chemistry and biochemistry [2, 3, 4] and medical resonance imaging (MRI) [5]. In all cases, the higher the spin polarization, the higher the desired signal. The spin-polarization P induced by a magnetic field at room temperature (for example, in medical imaging) is usually limited to no more than $P \sim 10^{-5}$, therefore, spin-polarized molecules with polarizations near unity can enhance MRI signals by several orders of magnitude. Furthermore, it is known that complete nuclear polarization increases the fusion cross section for the D-T and D- ^3He reactions by $\sim 50\%$ [6], and may increase the reactor efficiency by $\sim 75\%$ [7]. Additionally, it was predicted recently that spin-polarized D and T nuclei can reduce the minimum startup tritium inventory by more than an order of magnitude [8]. Finally, a first demonstration of polarization persistence in a laser-induced plasma was performed very recently [9], which is an important step for showing that spin polarization can survive in the plasma on timescales sufficient to benefit laser-induced fusion reactions.

However, methods for producing highly spin-polarized molecules are limited both by the quantity of molecules produced and by their purity, needed for magnetic resonance enhancement or polarized fusion applications. Dynamic nuclear polarization (DNP) and cryogenic cooling are the only methods that are routinely used to produce spin-polarized molecules in macroscopic quantities. DNP uses highly-polarized unpaired electrons in free radicals at low temperature in a magnetic field, to transfer this polarization to the nuclear spins of the target sample [10]. However, the free radicals need to be removed for medical applications, which is a difficult step that limits the applicability of the technique. Similarly, cryogenic cooling has been used to produce spin-polarized D_2 at a polarization of about 20%. The total production rates and polarizations are sufficient for proof-of-principle experiments, but otherwise are too small for the requirement of a nuclear fusion reactor: a $\sim 1 \text{ GW}$ nuclear reactor would require production rates of at least $\sim 10^{21} \text{ s}^{-1}$ [11, 12, 13].

*Corresponding author

Email address: ptr@ies1.forth.gr (T. Peter Rakitzis)

The Stern-Gerlach spin-separation technique, and spin-exchange optical pumping, are limited to microscopic production rates of $\sim 10^{17} \text{ s}^{-1}$ ($\sim 1 \mu\text{mol s}^{-1}$) for atoms [14, 15], and many orders of magnitude lower for molecules [16, 17]. These microscopic production rates are small and expensive for medical applications, and insufficient for nuclear fusion applications.

An alternative method for the production of spin-polarized molecules from the infrared (IR) excitation of molecular beams [18, 19] has been demonstrated [20, 21, 22]. In this method, the rotational angular momentum of the molecules is polarized in a rovibrational transition, and this polarization is transferred to the nuclear spin via the hyperfine interaction, on the timescale of about 10–100 μs (for spin-1/2 nuclei; higher spins can be polarized more quickly). The polarization can then be frozen in the molecular nuclei by stopping the spin-rotation interaction, either by photodissociating the molecule, turning on a magnetic field, or freezing the molecule at a surface (and stopping the molecular rotation).

This IR-excitation method can then produce orders-of-magnitude more spin-polarized molecules than the Stern-Gerlach spin-separation beam technique, for the following reasons. Both these beam techniques have production rates given by the product of the beam parameters $A\rho v$, where A is the cross-sectional area, ρ is the molecule number density, and v is the beam velocity. For the Stern-Gerlach method, the largest spin-polarized H-atom production rate of $A\rho v \sim 5 \times 10^{16} \text{ H/s}$ was achieved with $A \sim 1 \text{ cm}^2$, $\rho \sim 2 \times 10^{11} \text{ H/cm}^3$, and $v \sim 2.5 \times 10^5 \text{ cm/s}$ [6]. The beam density ρ or area A cannot be increased, without degrading the polarization from diminished spin separation, and v is determined by the supersonic beam expansion. For spin separation of molecules, the densities are about 3 orders of magnitude lower, as the nuclear magnetic moments are about 3 orders smaller than those of electrons. In contrast, the IR excitation method does not require spin separation, as polarization transfer through hyperfine beating occurs within each molecule, on a timescale 3–4 orders of magnitude faster than spin separation. Therefore, the beam densities ρ can be at least 3–4 orders higher, and the beam area A can be 1–2 orders larger, allowing beam production rates of $\sim 10^{22} \text{ s}^{-1}$. Recently, the authors have proposed the IR excitation of such formaldehyde (CH_2O) and formic acid (CH_2O_2) beams for the production of spin-polarized H_2 isotopes [23], at production rates of $\sim 10^{20} \text{ s}^{-1}$, limited by commercially available tabletop IR lasers with photon production rates of $\sim 10^{21} \text{ s}^{-1}$.

2. Description of the method

Here, we present a proposal for a general method for the production of spin-polarized small molecules, through the rotational excitation of molecular beams with microwaves. This method promises significantly higher production rates of spin-polarized molecules, as 10 W of microwaves in the 15 to 150 GHz range corresponds to polarized photon production rates of 10^{23} – 10^{24} s^{-1} , which is the limiting rate for spin-polarized molecule production. These rates are sufficient for medical-imaging and polarized-fusion applications. We describe methods for the polarization of isotopes of several small molecules: HD, DT, O_2 , NO, N_2O , CO, and H_2S_2 . The first six will be trapped directly after polarization onto a cold surface, whereas H_2S_2 is unstable and will be dissociated to yield and trap spin-polarized H_2 isotopes.

We note that the ability to rotationally excite some of these molecules near the 150 GHz range, or the rovibrational excitation of HD and DT with tunable narrowband infrared light, in macroscopic quantities, has been improved by recent improvements in microwave amplifiers and IR laser sources. Furthermore, we employ Stimulated Raman adiabatic passage (STIRAP) for IR excitation schemes, or π -pulses for microwave excitation schemes, that allow 100% population transfer from the ground state to the target excited state. The particular schemes utilized depends on the nuclear spins and rotational constants of the molecule. We first give a general description of the excitation schemes of molecular beams (and shown in Fig. 1), before giving specific details for the molecules HD, DT, O_2 , NO, N_2O , CO, and H_2S_2 :

1. Production of a molecular beam expansion, with a production rate of up to $\sim 10^{23} \text{ s}^{-1}$, which cools the rotational population to predominantly the lowest molecular rotational state ($J = 0$) [24, 25].
2. Circularly polarized microwave or IR beams, transfer ideally 100% of the molecules from the ground state to specific rovibrational states $|v J m_J\rangle$, from which subsequently the rotational polarization is transferred to the nuclear spin. In some cases more than one excitation and polarization-transfer step is needed.
3. After the nuclear spins are polarized, the hyperfine beating can be stopped, when the molecular beam enters a region with a sufficiently large magnetic field [26].

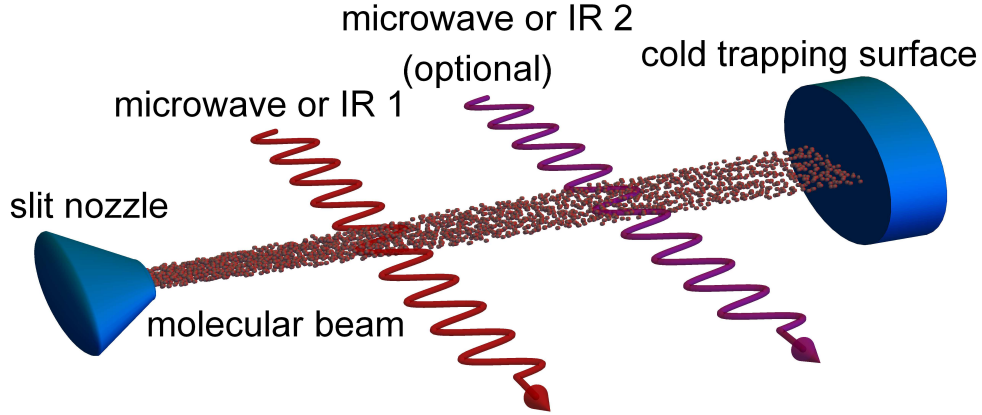


Figure 1: Sketch of the experimental setup. A cool molecular beam is excited to the state $|v J m_J\rangle$ —i.e., rotationally polarized—via microwave or IR radiation. This polarization is subsequently transferred to the nuclear spin. Additional excitation and polarization-transfer steps may be required. Finally, the polarized beam is collected on a cold surface.

4. The polarized molecular beam is finally collected and stored at a cold surface [27].

In this way, macroscopic production rates of spin-polarized HD, DT, O₂, NO, N₂O, CO molecules can be achieved in excess of $\sim 10^{21} \text{ s}^{-1}$.

3. Spin-polarization dynamics in HD, DT, O₂, NO, N₂O, ¹³CO, and H₂S₂

3.1. HD and DT

Figure 2 shows the excitation scheme adopted for the HD and DT molecules, utilizing an excited rovibrational state with $J = 2$. First, the system is pumped from the ground state $|0 0 0\rangle$ to the excited rovibrational state $|v' 2 2\rangle$ using two right circularly polarized laser beams. Due to hyperfine interactions, the population of this state redistributes among all m_J states, leading to the emergence of nuclear polarization. At time $t = t_1$, when the population of the $m_J = -1$ state reaches a minimum, the $m_J = 0, 1, 2$ states are repumped to the ground state, as depicted in Fig. 2(c). This ground state retains the induced nuclear polarization, as it does not exhibit hyperfine beating. Finally, the molecules can adhere to the cold surface, having no residual internal energy.



Figure 2: Excitation-polarization scheme for HD or DT via a $J = 2$ state. (a) Initial excitation from the lowest rovibrational state to $|v' 2 2\rangle$ at $t = 0$. (b) Redistribution of population among all m_J states until $t = t_1$, when the $m_J = -1$ population reaches a minimum. (c) At $t = t_1$, the $m_J = 0, 1, 2$ states are selectively repumped to the ground state, preserving the developed nuclear polarization.

The transfer of rotational angular momentum polarization to the nuclear spins in HD and DT molecules is enabled

through hyperfine interactions, which are described by the effective hyperfine Hamiltonian [28, 29, 30]:

$$H/h = -c_{p/t}\mathbf{I}_{p/t} \cdot \mathbf{J} - c_d\mathbf{I}_d \cdot \mathbf{J} + \frac{5d_1}{(2J-1)(2J+3)}\left[\frac{3}{2}(\mathbf{I}_{p/t} \cdot \mathbf{J})(\mathbf{I}_d \cdot \mathbf{J}) + \frac{3}{2}(\mathbf{I}_d \cdot \mathbf{J})(\mathbf{I}_{p/t} \cdot \mathbf{J}) - \mathbf{I}_{p/t} \cdot \mathbf{I}_d\mathbf{J}^2\right] \\ + \frac{5d_2}{(2J-1)(2J+3)}\left[3(\mathbf{I}_d \cdot \mathbf{J})^2 + \frac{3}{2}(\mathbf{I}_d \cdot \mathbf{J}) - \mathbf{I}_d^2\mathbf{J}^2\right], \quad (1)$$

where H/h is given in frequency units. The rotational angular momentum operator \mathbf{J} as well as the proton/triton ($\mathbf{I}_{p/t}$) and deuteron (\mathbf{I}_d) spin operators are considered dimensionless. The first two terms represent the nuclear spin-rotation interactions. The third term corresponds to the direct spin-spin magnetic interaction between the two nuclei, while the fourth term accounts for the interaction of the electric quadrupole moment of the deuteron.

We consider the excited vibrational state $v' = 2$. The theoretical values of hyperfine constants are [29, 30]: $c_p = 82.32$ kHz, $c_d = 12.64$ kHz, $d_1 = 16.521$ kHz, $d_2 = -21.793$ kHz for HD, and $c_t = 49.734$ kHz, $c_d = 7.158$ kHz, $d_1 = 18.095$ kHz, $d_2 = -22.135$ kHz for DT. The matrix representation of the hyperfine Hamiltonian can be readily obtained in the uncoupled basis $|J m_J, I_d m_d, I_p m_p\rangle = |J m_J\rangle \otimes |I_d m_d\rangle \otimes |I_p m_p\rangle$, thanks to its explicit structure (Eq. (1)). Since in our case $J = 2$, $I_d = 1$, and $I_p = 1/2$ are fixed, we simplify the notation to $|m_J, m_d, m_p\rangle$. This yields 30 state vectors which are employed for describing the system's spin state. Furthermore, we assume that during each optical pumping step, the radiation field affects only the rotational angular momentum, leaving the nuclear spin projections unchanged. For instance, when the system is initially pumped into the $|v' = 2, J = 2, m_J = 2\rangle$ state, its initial hyperfine state is taken to be a statistical mixture of the six equally weighted states: $|m_J = +2, m_d = 0, \pm 1, m_p = \pm 1/2\rangle$. Diagonalizing the Hamiltonian matrix provides the eigenenergies and facilitates the construction of the unitary time-evolution operator, $U = e^{-iHt/\hbar}$, used to calculate the time-evolved state vectors $|m_J, m_d, m_p\rangle_t$ at any given time t (for more details, see [26]).

From these, we can compute transition probabilities between initial and final states and evaluate the expectation values of the z -components of the relevant angular momentum operators— J_z , $I_{d,z}$, and $I_{p,z}$. As these operators are considered dimensionless and satisfy, e.g., $J_z|m_J, m_d, m_p\rangle = m_J|m_J, m_d, m_p\rangle$ (similarly for $I_{d,z}$ and $I_{p,z}$), we simplify notation by denoting the corresponding expectation values as $\langle m_J \rangle$, $\langle m_d \rangle$, and $\langle m_{p/t} \rangle$. Further details and explicit definitions regarding this framework can be found elsewhere [26].

A single polarization cycle can produce moderate nuclear polarization. However, by repeating this cycle multiple times, it is possible to achieve high nuclear polarization with effectively no population loss. A cycle is considered completed after the selective repumping of the $m_J = 0, 1, 2$ state populations to the ground state, i.e., upon completion of the third step in Fig. 2. The cycle duration is taken to be equal to the free evolution period during the second step of Fig. 2. The next cycle begins immediately after the previous one ends, with no time delay. While a delay could easily be incorporated into the model, it is set to zero in this example. Furthermore, polarization damping between cycles is neglected, and the laser field is assumed to have no direct effect on the nuclear spins.

Cycle	Duration		Deuteron Polarization		Proton/Triton Polarization		Population Loss	
	HD	DT	HD	DT	HD	DT	HD	DT
1	4.52 μ s	6.44 μ s	59.4%	57.4%	20.0%	30.1%	0.3%	0.3%
2	4.52 μ s	6.04 μ s	77.1%	80.4%	46.9%	58.7%	0.07%	0.03%
3	7.85 μ s	6.04 μ s	86.9%	90.7%	72.1%	76.4%	0.01%	0.002%
4	4.56 μ s	5.28 μ s	92.6%	95.5%	80.3%	87.4%	0.0007%	0.0005%
5	3.00 μ s	5.44 μ s	94.7%	97.7%	91.8%	93.2%	0.002%	0.0001%
6	2.84 μ s	5.52 μ s	96.4%	98.8%	96.2%	96.4%	0.0008%	0.00002%

Table 1: Parameters of successive polarization cycles in HD and DT.

Table 1 summarizes the key parameters characterizing each polarization cycle in HD and DT. The duration of each cycle is tailored to its specific objective. In particular, the first four cycles in HD are timed to minimize population loss from the $|2, 2, -1\rangle$ state, while the final two cycles are optimized to further enhance proton polarization—by which point population losses have already been reduced to a negligible level. In the case of DT, the first three cycles serve to reduce population loss, and the remaining three are dedicated to maximizing triton polarization. After six polarization

cycles, the nuclear polarization in both molecules exceeds 96%, with minimal population loss. Alternative timing strategies may be employed depending on the desired final polarization.

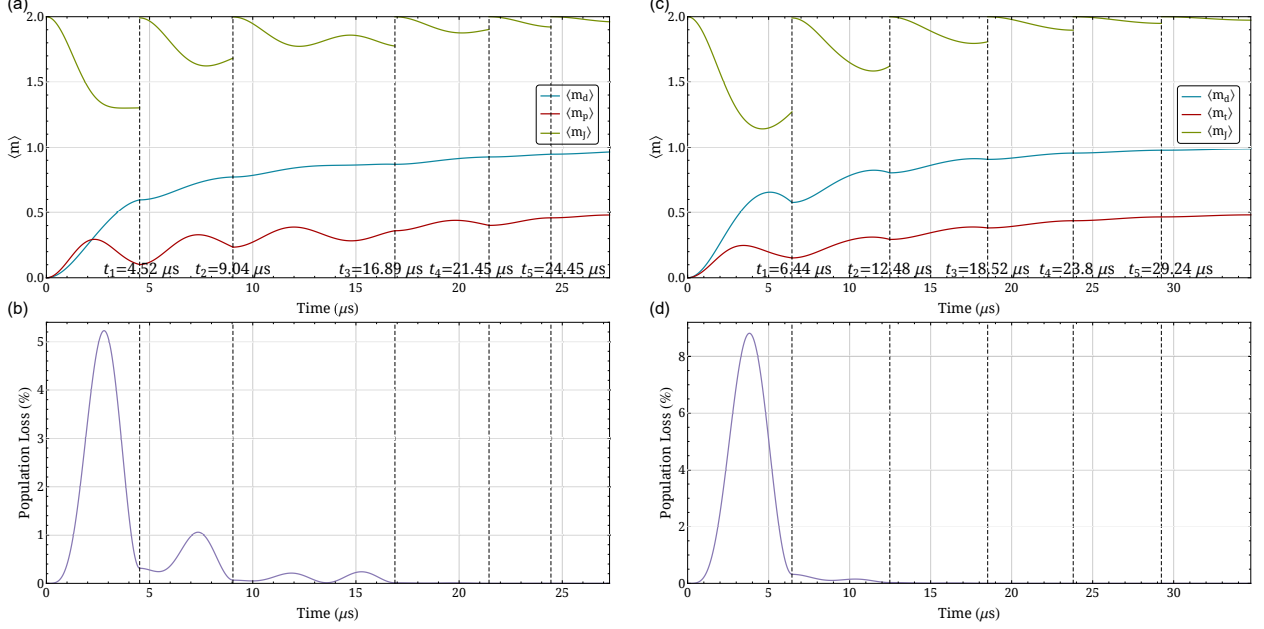


Figure 3: Time evolution of expectation values of the rotational angular momentum projection $\langle m_J \rangle$ and nuclear spin projections $\langle m_d \rangle$ and $\langle m_{p/t} \rangle$ in panels (a) and (c), and of population loss in panels (b) and (d), over six polarization cycles in HD and DT. The plots correspond to the $|v' = 2, J = 2\rangle$ excited state, and therefore the slight reduction in nuclear polarization due to the repumping process at the end of each cycle is not depicted.

Figure 3 illustrates the time evolution of the expectation values of the nuclear spin projections $\langle m_d \rangle$ and $\langle m_{p/t} \rangle$ along with the population loss, over six polarization cycles. It is important to note that these values reflect the excited-state properties at the end of the second step in each cycle (see Fig. 2(b)), i.e., just before repumping to the ground state. The corresponding nuclear polarization values after repumping—i.e., at the end of each complete cycle—are listed in Tab. 1 and are slightly lower than those shown in the figure.

3.2. O_2

Next, we consider the case of molecular oxygen O_2 , an open-shell molecule with two unpaired electrons. In particular, its electronic ground state $^3\Sigma_g^-$ has been extensively studied with microwave spectroscopy techniques. This state has a total electron spin of $S = 1$ and orbital angular momentum projection of $\Lambda = 0$. The angular momentum quantum number for rotation is denoted by N , which together with the electron spin, forms the total angular momentum J . Due to symmetry constraints N can only take odd integer values. Within the $N = 1$ rotational level, we consider the excitation $|J = 0, m_J = 0\rangle \rightarrow |J = 1, m_J = 1\rangle$. This results in a 50% polarization for the total electron spin and 50% rotational polarization, both of which remain time-independent. A subsequent transition, $|1, 1\rangle \rightarrow |2, 2\rangle$, still within $N = 1$, can achieve an electron polarization close to 100%. Specifically, the electron polarization oscillates between 89.8% and 100% with a period of 2.1 ps. The time-averaged electron spin polarization is approximately 95%.

The fine-structure effective Hamiltonian matrix elements (in frequency units) are explicitly derived in [31]. Below we summarize them, focusing only on the variation in N :

$$H^{N=J} = \langle N = J | H | N = J \rangle = BJ(J+1) - DJ^2(J+1)^2 + HJ^3(J+1)^3 - \gamma - \gamma_D J(J+1) - \gamma_H J^2(J+1)^2 + \frac{2}{3}[\lambda + \lambda_D J(J+1) + \lambda_H J^2(J+1)^2] \quad (2)$$

$$\begin{aligned}
H^{J-1,J-1} = \langle N = J - 1 | H | N = J - 1 \rangle &= B J(J - 1) - D J^2(J - 1)^2 \\
&+ H J^3(J - 1)^3 + [\gamma + \gamma_D J(J - 1) + \gamma_H J^2(J - 1)^2](J - 1) \\
&+ [\lambda + \lambda_D J(J - 1) + \lambda_H J^2(J - 1)^2] \left(\frac{2}{3} - \frac{2J}{2J + 1} \right)
\end{aligned} \tag{3}$$

$$\begin{aligned}
H^{J+1,J+1} = \langle N = J + 1 | H | N = J + 1 \rangle &= B(J + 2)(J + 1) - D(J + 2)^2(J + 1)^2 \\
&+ H(J + 2)^3(J + 1)^3 - [\gamma + \gamma_D(J + 2)(J + 1) + \gamma_H(J + 2)^2(J + 1)^2] \\
&\times (J + 2) + [\lambda + \lambda_D(J + 2)(J + 1) + \lambda_H(J + 2)^2(J + 1)^2] \times \left(\frac{2}{3} - \frac{2(J + 1)}{2J + 1} \right)
\end{aligned} \tag{4}$$

$$H^{J-1,J+1} = \langle N = J - 1 | H | N = J + 1 \rangle = H^{J+1,J-1} = [\lambda + \lambda_D(J^2 + J + 1) + \lambda_H(J^2 + J + 1)^2] \frac{2\sqrt{J(J+1)}}{2J + 1}, \tag{5}$$

where λ and γ are the spin-spin and spin-rotation constants, respectively. Subscripts D and H denote the first and second order centrifugal distortion constants. The constants B , D , and H correspond to the rotational constant and its first and second order centrifugal distortion terms, respectively. The measured values of these spectroscopic parameters for the electronic ground state $^3\Sigma_g^-$ of O_2 are listed in Tab. 2, taken from [32].

The evaluation of the above results involves the Clebsch-Gordan decomposition of the total angular momentum \mathbf{J} into the rotation quantum number \mathbf{N} and the total electron spin \mathbf{S} :

$$|Nm_N, Sm_S\rangle = \sum_{J=|N-S|, m_J=-J}^{J=N+S, m_J=J} \langle Jm_J | Nm_N, Sm_S \rangle |Jm_J\rangle, \tag{6}$$

where $\langle Jm_J | Nm_N, Sm_S \rangle = \langle Nm_N, Sm_S | Jm_J \rangle$ are the Clebsch-Gordan coefficients. This basis transformation allows for expressing the Hamiltonian matrix in the uncoupled representation, where the electron spin polarization is directly accessible.

Parameter	Frequency in MHz
B	43100.44276
D	145.1271×10^{-3}
H	49×10^{-9}
λ	-59501.3438
λ_D	-58.3680×10^{-3}
λ_H	-290.8×10^{-9}
γ	-252.58634
γ_D	-243.42×10^{-6}
γ_H	-1.46×10^{-9}

Table 2: Measured spectroscopic parameters for the electronic ground state $^3\Sigma_g^-$ of O_2 , from [32].

3.3. NO

Nitric oxide (NO) is a stable free radical with one unpaired electron and a doublet electronic ground state, $^2\Pi$. The energy separation between the lower $^2\Pi_{1/2}$ state and the upper $^2\Pi_{3/2}$ is about 123 cm^{-1} [33, 34]. In this study, both nitrogen isotopes, ^{14}N ($I = 1$) and ^{15}N ($I = 1/2$), are considered following the excitation scheme illustrated in Fig. 4. As a result, the system is initially prepared in the $|1/2 \ 1/2\rangle$ and $|3/2 \ 3/2\rangle$ states with equal population and zero nuclear spin polarization. The corresponding Hamiltonian matrix elements (in frequency units), as given in [35], are

listed below:

$$\begin{aligned} \langle I, {}^2\Pi_{1/2} J'; F \pm |H|I, {}^2\Pi_{1/2} J; F \pm \rangle = & \left[-\frac{1}{2}A_{eff} - \frac{1}{2}A_{D,eff}(X+1) + B_{eff}(X+1) - D[(X+1)^2 + X] \right. \\ & \pm \frac{1}{2}(-1)^{J-1/2} [lp + p_D(X+1)] \left(J + \frac{1}{2} \right) + 2[q + q_D(X+1)] \left(J + \frac{1}{2} \right) \Big] \delta_{J',J} \\ & + G(I, J', J, F) \left[(-1)^{J'-1/2} \begin{pmatrix} J' & 1 & J \\ -\frac{1}{2} & 0 & \frac{1}{2} \end{pmatrix} \left(a - \frac{b+c}{2} + \delta_{J',J} 2XC_I \right) \right. \\ & \left. \mp \begin{pmatrix} J' & 1 & J \\ \frac{1}{2} & -1 & \frac{1}{2} \end{pmatrix} \frac{d + \delta_{J',J} X d_D}{\sqrt{2}} \right] + Q(I, J', J, F) (-1)^{J'-1/2} \begin{pmatrix} J' & 2 & J \\ -\frac{1}{2} & 0 & \frac{1}{2} \end{pmatrix} \frac{eQq_1}{4} \end{aligned} \quad (7)$$

$$\begin{aligned} \langle I, {}^2\Pi_{3/2} J'; F \pm |H|I, {}^2\Pi_{3/2} J; F \pm \rangle = & \left[\frac{1}{2}A_{eff} + \frac{1}{2}A_{D,eff}(X-1) + B_{eff}(X-1) - D[(X-1)^2 + X] \right. \\ & \pm \frac{1}{2}(-1)^{J-1/2} q_D X \left(J + \frac{1}{2} \right) \Big] \delta_{J',J} \\ & + G(I, J', J, F) (-1)^{J'-3/2} \begin{pmatrix} J' & 1 & J \\ -\frac{3}{2} & 0 & \frac{3}{2} \end{pmatrix} \left(a + \frac{b+c}{2} + \delta_{J',J} \frac{2}{3} XC_I \right) \\ & + Q(I, J', J, F) (-1)^{J'-3/2} \begin{pmatrix} J' & 2 & J \\ -\frac{3}{2} & 0 & \frac{3}{2} \end{pmatrix} \frac{eQq_1}{4} \end{aligned} \quad (8)$$

$$\begin{aligned} \langle I, {}^2\Pi_{3/2} J'; F \pm |H|I, {}^2\Pi_{1/2} J; F \pm \rangle = & \left[-B_{eff} X^{1/2} + 2DX^{3/2} \mp \frac{1}{2}[q + q_D(X+1)] \left(J + \frac{1}{2} \right) X^{1/2} \right] \delta_{J',J} \\ & - G(I, J', J, F) (-1)^{J'-3/2} \begin{pmatrix} J' & 1 & J \\ -\frac{3}{2} & 1 & \frac{1}{2} \end{pmatrix} \frac{b \pm \delta_{J',J} (-1)^{J-1/2} \left(J + \frac{1}{2} \right) C'_I}{\sqrt{2}} \\ & \mp Q(I, J', J, F) \begin{pmatrix} J' & 2 & J \\ \frac{3}{2} & -2 & \frac{1}{2} \end{pmatrix} \frac{eQq_2}{4\sqrt{6}}, \end{aligned} \quad (9)$$

where $X = J(J+1) - \frac{3}{4}$ and

$$G(I, J', J, F) = (-1)^{I+J'+F} \begin{Bmatrix} F & J' & I \\ 1 & I & J \end{Bmatrix} \sqrt{I(I+1)(2I+1)(2J'+1)(2J+1)} \quad (10)$$

$$Q(I, J', J, F) = (-1)^{I+J'+F} \begin{Bmatrix} F & J' & I \\ 1 & I & J \end{Bmatrix} \sqrt{\frac{(I+1)(2I+1)(2I+3)}{I(2I-1)}} (2J'+1)(2J+1). \quad (11)$$

The total angular momentum \mathbf{F} arises from the coupling of \mathbf{J} and \mathbf{I} . The signs \pm in the bra-ket notation indicate the parity of the states. The experimental values of all spectroscopic constants are summarized in Tab. 3. The above matrix elements yield a Hamiltonian in the so-called coupled representation. To compute observables such as the average rotational angular momentum projection and nuclear spin projection, a basis transformation is performed to express the Hamiltonian in the uncoupled representation. This allows direct evaluation of these quantities using a code similar to Sec. 3.1. In practice, the Hamiltonian matrix size in the uncoupled basis is 72×72 for ^{14}NO and 48×48 for ^{15}NO .

Figure 5 shows the time evolution of the average nuclear spin and rotational angular momentum projection for the ^{14}N (a) and ^{15}N (b) isotopes. In the case of ^{14}N , the nuclear polarization reaches 61.1% at 22.2 ns after excitation, whereas for ^{15}N , it reaches 84.5% at 28.8 ns.

3.4. N_2O

Nitrous oxide (N_2O) is a linear molecule with nitrogen as the central atom, making the two nitrogen nuclei distinguishable due to their nonidentical interactions. We label the outer nitrogen and central nitrogen nuclei with indices 1 and 2, respectively. For $^{14}\text{N}_2\text{O}$, we consider the excitation sequence $|J=0, m_J=0\rangle \rightarrow |1, 1\rangle \rightarrow |2, 2\rangle$, selected to achieve high polarization, as it involves two spin-1 nuclei.

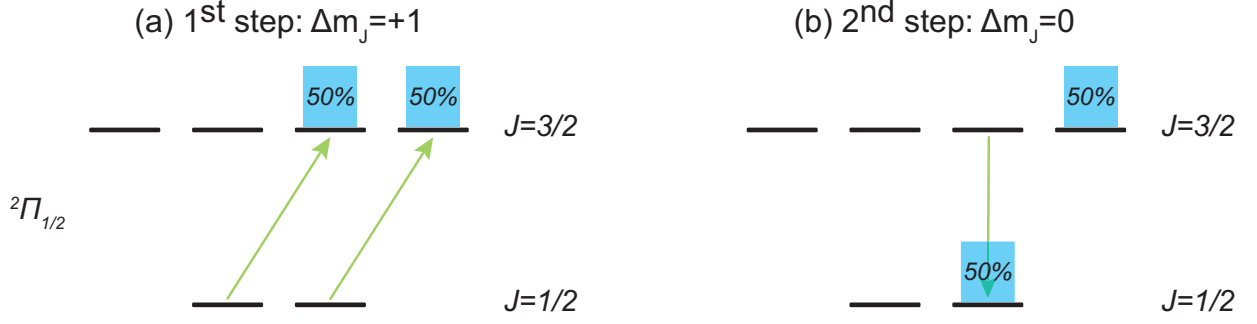


Figure 4: Excitation-polarization scheme for the $^2\Pi_{1/2}$ state of NO: (a) Transitions with $\Delta m_J = 1$: $|J = 1/2 m_J = -1/2\rangle \rightarrow |3/2 1/2\rangle$ and $|1/2 1/2\rangle \rightarrow |3/2 3/2\rangle$. (b) Transition with $\Delta m_J = 0$: $|3/2 1/2\rangle \rightarrow |1/2 1/2\rangle$.

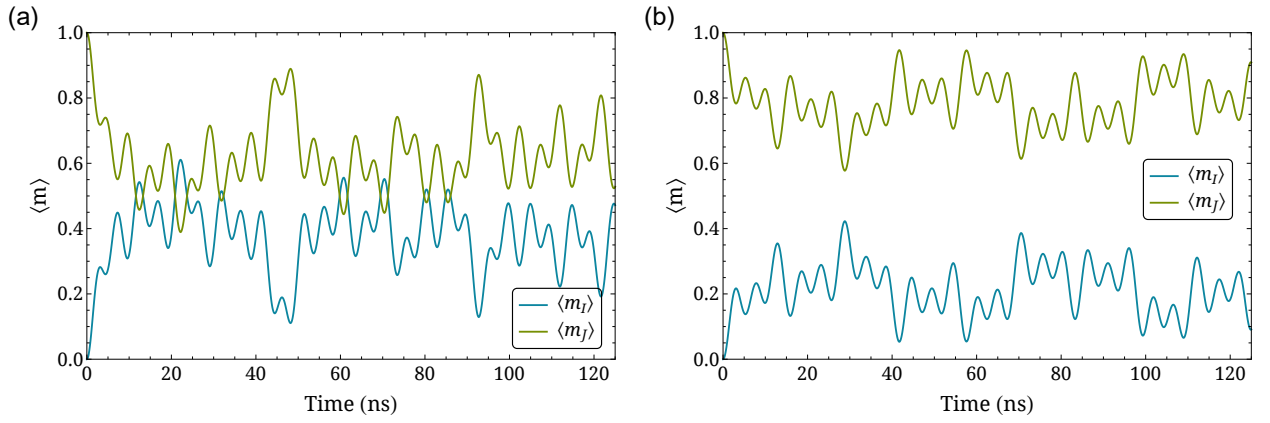


Figure 5: Time evolution of the average projections of rotational angular momentum $\langle m_J \rangle$ (green) and nuclear spin $\langle m_I \rangle$ (blue) for the molecules: (a) ^{14}NO and (b) ^{15}NO .

Parameter	Frequency in MHz	
	¹⁴ N ¹⁵ O	¹⁵ N ¹⁴ O
A_{eff}	3691619	3691683
$A_{D,eff}$	5.497	5.120
B_{eff}	50847.7988	49050.532
D	0.164073	0.1525
p	350.37517	337.9627
p_D	0.000086	0.00011
q	2.83713	2.64012
q_D	0.000044	0.0000379
a	84.2155	-118.143
b	42.099	-59.024
c	-58.989	82.725
d	112.5972	-157.9474
d_D	0.00016	-
C_I	0.01242	-0.01622
C'_I	0.0039	-0.0055
eQq_1	-1.8581	-
eQq_2	23.153	-

Table 3: Measured spectroscopic constants for the electronic ground states of ¹⁴N¹⁵O and ¹⁵N¹⁴O, as reported in [35].

The effective hyperfine Hamiltonian of ¹⁴N₂O, expressed in frequency units and following the sign convention of [36] for the spin-rotation terms, is given by:

$$\begin{aligned}
H/h = & -M_{N_1} \mathbf{I}_1 \cdot \mathbf{J} - M_{N_2} \mathbf{I}_2 \cdot \mathbf{J} + \frac{(eqQ)_{N_1}}{2I_1(2I_1-1)J(2J-1)} \left[3(\mathbf{I}_1 \cdot \mathbf{J})^2 + \frac{3}{2}(\mathbf{I}_1 \cdot \mathbf{J}) - \mathbf{I}_1^2 \mathbf{J}^2 \right] \\
& + \frac{(eqQ)_{N_2}}{2I_2(2I_2-1)J(2J-1)} \left[3(\mathbf{I}_2 \cdot \mathbf{J})^2 + \frac{3}{2}(\mathbf{I}_2 \cdot \mathbf{J}) - \mathbf{I}_2^2 \mathbf{J}^2 \right] \\
& + \frac{2D_{NN}}{(2J-1)(2J+3)} \left[\frac{3}{2}(\mathbf{I}_1 \cdot \mathbf{J})(\mathbf{I}_2 \cdot \mathbf{J}) + \frac{3}{2}(\mathbf{I}_2 \cdot \mathbf{J})(\mathbf{I}_1 \cdot \mathbf{J}) - \mathbf{I}_1 \cdot \mathbf{I}_2 \mathbf{J}^2 \right].
\end{aligned} \tag{12}$$

The first two terms describe the spin-rotation interaction. The next two terms account for the electric quadrupole interactions of the two nitrogen nuclei, and the final term represents the dipole spin-spin interaction between \mathbf{I}_1 and \mathbf{I}_2 . The experimentally reported hyperfine constants for ¹⁴N₂O [36], along with estimated values for ¹⁵N₂O are listed in Tab. 4. The values for ¹⁵N₂O are obtained by substituting the ¹⁴N g-factors with those of ¹⁵N and omitting the quadrupole interaction terms, as the nuclear spin of ¹⁵N is 1/2.

Parameter	Frequency in kHz	
	¹⁴ N ₂ O	¹⁵ N ₂ O
M_{N_1}	-2.35	3.30
M_{N_2}	-2.90	4.07
$(eqQ)_{N_1}$	-776.7	-
$(eqQ)_{N_2}$	-269.4	-
D_{NN}	0.436	0.858

Table 4: Hyperfine constants for ¹⁴N₂O and ¹⁵N₂O. The values for ¹⁴N₂O are adapted from [36], while those for ¹⁵N₂O are estimated based on molecular similarity and the ¹⁵N g-factor.

As shown in Fig. 6(a), the total nitrogen nuclear polarization in ¹⁴N₂O exceeds 57% at times 1.7 μs and 23.5 μs. For ¹⁵N₂O, a single excitation scheme $|00\rangle \rightarrow |11\rangle$ is considered due to its different total nuclear spin. The resulting hyperfine beatings, depicted in Fig. 6(b), indicate that the total nuclear polarization reaches 69.8% at 80.1 μs after excitation.

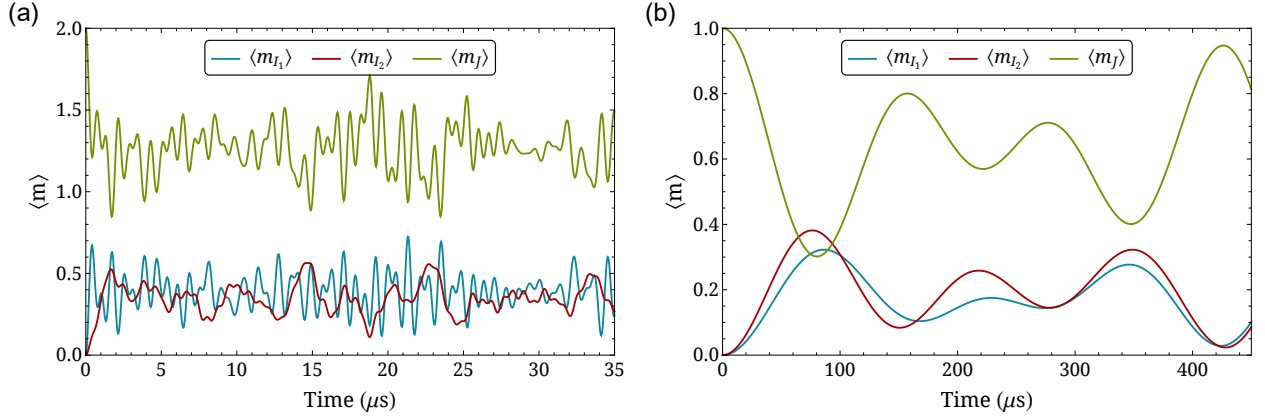


Figure 6: Time evolution of the average projections of rotational angular momentum $\langle m_J \rangle$ (green) and nitrogen nuclear spins $\langle m_{I_{1,2}} \rangle$ (blue and red) for the molecules: (a) $^{14}\text{N}_2\text{O}$ and (b) $^{15}\text{N}_2\text{O}$.

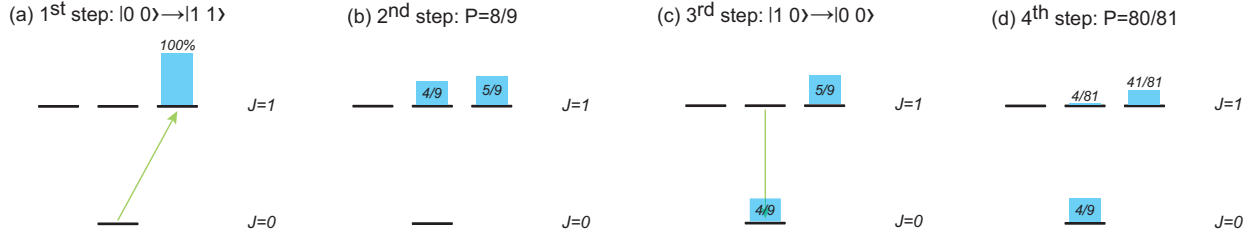


Figure 7: Excitation-polarization scheme for ^{13}CO : (a) Excitation from the ground state $|00\rangle$ to $|11\rangle$. (b) Free evolution for 10.2 μs , during which the nuclear polarization reaches its maximum value of 8/9. (c) De-excitation from $|10\rangle$ to $|00\rangle$. (d) Further free evolution for 10.2 μs , resulting in nuclear polarization of 80/81.

3.5. ^{13}CO

Carbon-13 monoxide (^{13}CO) exhibits the simplest hyperfine structure among the molecules considered in this work. Its interaction is limited to the coupling between the nuclear spin \mathbf{I} (with $I = 1/2$) and the rotational angular momentum \mathbf{J} . The corresponding nuclear spin-rotation constant has been experimentally determined to be 32.63 kHz [37]. Figure 7 illustrates a potential excitation scheme to achieve high nuclear polarization for the molecule. The system is initially excited from the ground state $|00\rangle$ to the $|11\rangle$ state (see Fig. 7(a)). After a free evolution of 10.2 μs (see Fig. 8(a)), the nuclear polarization reaches 8/9, as shown in Fig. 7(b). At this point, the populations of the $|10\rangle$ and $|11\rangle$ states are 4/9 and 5/9, respectively. Next, the $|10\rangle$ state is de-excited, transferring 4/9 of the total population to the ground state $|00\rangle$ (see Fig. 7(c)). Since the ground state exhibits no hyperfine beating, it retains its 100% nuclear polarization. Allowing the system to evolve for an additional 10.2 μs results in population redistribution among the $J = 1$ states, as illustrated in Fig. 7(d). These states exhibit a nuclear polarization of 44/45. Considering the fully nuclear-spin-polarized population of the ground state, the average nuclear polarization across the molecule reaches 80/81.

3.6. $\text{H}^{32}\text{S}^{34}\text{SH}$

Hydrogen disulfide (H_2S_2) is a symmetric molecule that is an almost accidentally prolate symmetric top based on its principal moments of inertia. When the sulfur nuclei are identical, the molecular symmetry restricts the total nuclear spin of the two hydrogen nuclei for different rotational levels, leading to ortho- and para-species associated with rotational levels of different symmetries [38]. Substituting one ^{32}S with ^{34}S (both isotopes have $I = 0$) breaks this symmetry, allowing all possible proton spin combinations for every rotational level J of $\text{H}^{32}\text{S}^{34}\text{SH}$ (which has a natural abundance of 8% [39]). Since the molecule's total nuclear spin arises solely from the two protons ($I_{1,2} = 1/2$), a single excitation $|00\rangle \rightarrow |11\rangle$ can efficiently transfer rotational angular momentum polarization to the nuclear spins.

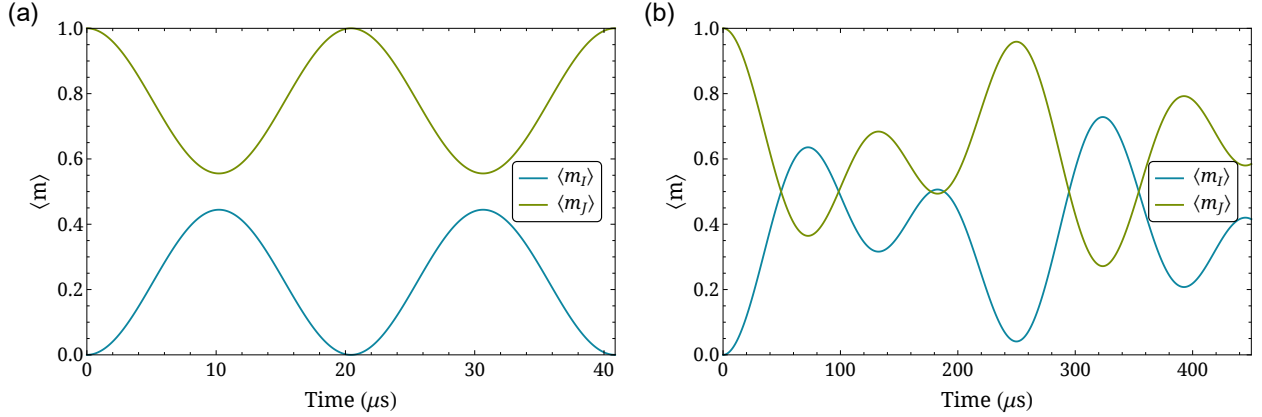


Figure 8: Time evolution of the average projections of rotational angular momentum $\langle m_J \rangle$ (green) and nuclear spin $\langle m_I \rangle$ (blue) for the molecules: (a) ^{13}CO and (b) $\text{H}^{32}\text{S}^{34}\text{SH}$.

The effective hyperfine Hamiltonian includes nuclear spin-rotation interactions and the dipole spin-spin interaction between the two protons, and can be written in frequency units as:

$$H/h = C_J(\mathbf{I}_1 \cdot \mathbf{J} + \mathbf{I}_2 \cdot \mathbf{J}) + \frac{D_J}{J(2J-1)} \left[\frac{3}{2}(\mathbf{I}_1 \cdot \mathbf{J})(\mathbf{I}_2 \cdot \mathbf{J}) + \frac{3}{2}(\mathbf{I}_2 \cdot \mathbf{J})(\mathbf{I}_1 \cdot \mathbf{J}) - \mathbf{I}_1 \cdot \mathbf{I}_2 J^2 \right], \quad (13)$$

where only the dipolar coupling constant, D_J can be reliably calculated from molecular geometry [40]. The spin-rotation constant C_J is estimated based on [41, 42, 43], providing a plausible order of magnitude in the absence of direct measurements. For the 1_{01} level, we estimate $C_{1_{01}} \sim -4$ kHz and calculate $D_{1_{01}} = 0.11$ kHz. Using the same methodology as for the other molecules, we simulate the resulting polarization beatings, as shown in Fig. 8(b). The total nuclear polarization reaches $\sim 64\%$ and $\sim 73\%$ at ~ 72 μs and ~ 323 μs , respectively.

4. Conclusion

We have presented methods for producing highly spin-polarized molecules, including HD, DT, O_2 , NO, N_2O , CO, and H_2S_2 . These approaches rely on the coherent excitation of molecular beams using microwave or infrared radiation, enabling polarization production rates in excess of 10^{21} s^{-1} . The techniques described here are general and can be extended to a wide range of other small molecules, offering promising prospects for applications in nuclear magnetic resonance and spin-polarized nuclear fusion.

Acknowledgments

This work was partially supported by the Hellenic Foundation for Research and Innovation (HFRI) and the General Secretariat for Research and Technology (GSRT), under grant agreement No. HFRI-FM17-3709 (project NUPOL). CSK acknowledges funding from the Deutsche Forschungsgemeinschaft (DFG, German Research Foundation)-533904660. We thank Ahmed Diallo and Jason F. Parisi for useful discussions.

References

- [1] E. Steffens and W. Haeberli, Rep. Prog. Phys. **66**, R02 (2003).
- [2] R. A. Green, R. W. Adams, S. B. Duckett, R. E. Mewis, D. C. Williamson, and G. G. Green, Prog. Nucl. Magn. Reson. Spectrosc. **67**, 1 (2012).
- [3] K. R. Keshari and D. M. Wilson, Chem. Soc. Rev. **43**, 1627 (2014).
- [4] M. H. Levitt, Annu. Rev. Phys. Chem. **63**, 89 (2012).
- [5] D. W. McRobbie, E. A. Moore, M. J. Graves, and M. R. Prince, *MRI from Picture to Proton*, 2nd ed. (Cambridge University Press, 2007).
- [6] G. Hupin, S. Quaglioni, and P. Navrátil, Nat. Commun. **10**, 351 (2019).

- [7] M. Temporal, V. Brandon, B. Canaud, J. Didelez, R. Fedosejevs, and R. Ramis, Nucl. Fusion **52**, 103011 (2012).
- [8] J. Parisi, A. Diallo, and J. Schwartz, Nucl. Fusion **64**, 126019 (2024).
- [9] C. Zheng, P. Fedorets, R. Engels, I. Engin, H. Glückler, C. Kannis, N. Schnitzler, H. Soltner, Z. Chitgar, P. Gibbon, L. Reichwein, A. Pukhov, B. Zielbauer, and M. Büscher, arXiv:2310.04184 .
- [10] J. H. Ardenkjær-Larsen, B. Fridlund, A. Gram, G. Hansson, L. Hansson, M. H. Lerche, R. Servin, M. Thaning, and K. Golman, Proc. Natl. Acad. Sci. U.S.A. **100**, 10158 (2003).
- [11] K. Grigoryev, N. Chernov, R. Engels, I. Ivanov, S. Kiselev, E. Komarov, L. Kotchenda, P. Kravtsov, L. Kroell, A. Martyushov, M. Marusina, M. Mikirtychyants, N. Nikolaev, F. Rathmann, H. P. gen Schieck, S. Sherman, H. Ströher, V. Trofimov, A. Vasilyev, and M. Vznuzdaev, J. Phys. Conf. Ser. **295**, 012168 (2011).
- [12] R. M. Kulsrud, Application of Polarized Nuclei to Fusion, in *Muon-Catalyzed Fusion and Fusion with Polarized Nuclei*, edited by B. Brunelli and G. G. Leotta (Springer US, Boston, MA, 1987) pp. 169–178.
- [13] R. W. Moir, Fusion Technol. **21**, 1475 (1992).
- [14] A. Nass, C. Baumgarten, B. Braun, G. Ciullo, G. Court, P. Dalpiaz, A. Golendukhin, G. Graw, W. Haeberli, M. Henoch, R. Hertenberger, N. Koch, H. Kolster, P. Lenisa, H. Marukyan, M. Raithel, D. Reggiani, K. Rith, M. Simani, E. Steffens, J. Stewart, P. Tait, and T. Wise, Nucl. Instrum. Methods Phys. Res., Sect. A **505**, 633 (2003).
- [15] B. Clasie, C. Crawford, J. Seely, W. Xu, D. Dutta, and H. Gao, Phys. Rev. A **73**, 020703 (2006).
- [16] T. Kravchuk, M. Reznikov, P. Tichonov, N. Avidor, Y. Meir, A. Bekkerman, and G. Alexandrowicz, Science **331**, 319 (2011).
- [17] D. A. Horke, Y.-P. Chang, K. Długołęcki, and J. Küpper, Angew. Chem. Int. Ed. **53**, 11965 (2014).
- [18] T. P. Rakitzis, Phys. Rev. Lett. **94**, 083005 (2005).
- [19] L. Rubio-Lago, D. Sofikitis, A. Koubenakis, and T. P. Rakitzis, Phys. Rev. A **74**, 042503 (2006).
- [20] D. Sofikitis, L. Rubio-Lago, M. R. Martin, D. J. A. Brown, N. C.-M. Bartlett, R. N. Zare, and T. P. Rakitzis, Phys. Rev. A **76**, 012503 (2007).
- [21] N. C.-M. Bartlett, D. J. Miller, R. N. Zare, A. J. Alexander, D. Sofikitis, and T. P. Rakitzis, Phys. Chem. Chem. Phys. **11**, 142 (2009).
- [22] N. C.-M. Bartlett, J. Jankunas, R. N. Zare, and J. A. Harrison, Phys. Chem. Chem. Phys. **12**, 15689 (2010).
- [23] C. S. Kannis and T. P. Rakitzis, Chem. Phys. Lett. **784**, 139092 (2021).
- [24] S. Grieser, D. Bonaventura, P. Brand, C. Hargens, B. Hetz, L. Leßmann, C. Westphäliger, and A. Khokaz, Nucl. Instrum. Methods Phys. Res., Sect. A **906**, 120 (2018).
- [25] B. Schlimme, S. Aulenbacher, P. Brand, M. Littich, Y. Wang, P. Achenbach, M. Ball, J. Bernauer, M. Biroth, D. Bonaventura, D. Bosnar, S. Caiazza, M. Christmann, E. Cline, A. Denig, M. Distler, L. Doria, P. Eckert, A. Esser, I. Frišići, S. Gagneur, J. Geimer, S. Grieser, P. Güllker, P. Herrmann, M. Hoek, S. Kegel, J. Kelsey, P. Klag, A. Khokaz, M. Kohl, T. Kolar, M. Lauß, L. Leßmann, S. Lunkenheimer, J. Marekovič, D. Markus, M. Mauch, H. Merkel, M. Mihovilović, R. Milner, J. Müller, U. Müller, T. Petrovič, J. Pochodzalla, J. Rausch, J. Schlaadt, H. Schürg, C. Sfienti, S. Širca, R. Spreckels, S. Stengel, Y. Stöttinger, C. Szyszka, M. Thiel, S. Vestrick, and C. Vidal, Nucl. Instrum. Methods Phys. Res., Sect. A **1013**, 165668 (2021).
- [26] C. S. Kannis, G. E. Katsoprinakis, D. Sofikitis, and T. P. Rakitzis, Phys. Rev. A **98**, 043426 (2018).
- [27] T. R. Govers, L. Mattera, and G. Scoles, J. Chem. Phys. **72**, 5446 (1980).
- [28] N. F. Ramsey and H. R. Lewis, Phys. Rev. **108**, 1246 (1957).
- [29] H. Jóźwiak, H. Cybulski, and P. Weislo, J. Quant. Spectrosc. Radiat. Transfer **253**, 107171 (2020).
- [30] H. Jóźwiak, H. Cybulski, and P. Weislo, J. Quant. Spectrosc. Radiat. Transfer **256**, 107255 (2020).
- [31] R. Larsson, B. Lankhaar, and P. Eriksson, J. Quant. Spectrosc. Radiat. Transfer **224**, 431 (2019).
- [32] B. J. Drouin, S. Yu, C. E. Miller, H. S. Müller, F. Lewen, S. Brünken, and H. Habara, J. Quant. Spectrosc. Radiat. Transfer **111**, 1167 (2010).
- [33] A. C. J.M. Brown and F. Honey, Mol. Phys. **23**, 287 (1972).
- [34] G. W. A.H. Saleck and K. Yamada, Mol. Phys. **76**, 1443 (1992).
- [35] K. Y. A.H. Saleck and G. Winnewisser, Mol. Phys. **72**, 1135 (1991).
- [36] K. H. Casleton and S. G. Kukolich, J. Chem. Phys. **62**, 2696 (1975).
- [37] G. Klapper, F. Lewen, R. Gendriesch, S. Belov, and G. Winnewisser, J. Mol. Spectrosc. **201**, 124 (2000).
- [38] G. Winnewisser, M. Winnewisser, and W. Gordy, J. Chem. Phys. **49**, 3465 (1968).
- [39] J. Behrend, P. Mittler, G. Winnewisser, K. Yamada, and M. Winnewisser, J. Mol. Spectrosc. **141**, 265 (1990).
- [40] G. Winnewisser and K. Yamada, Vib. Spectrosc. **1**, 263 (1991).
- [41] A. Saleck, M. Tanimoto, S. Belov, T. Klaus, and G. Winnewisser, J. Mol. Spectrosc. **171**, 481 (1995).
- [42] A. H. Saleck and G. Winnewisser, Z. Naturforsch. A **50**, 1191 (1995).
- [43] G. Cazzoli and C. Pizzarini, J. Mol. Spectrosc. **298**, 31 (2014).